JOM
https://doi.org/10.1007/s11837-022-05462-2

Effect of Microtextured Region Stereology on Crack Growth Lifetime Predictions in Ti-6Al-4V

J.R. JAMES ,[1,5] R. JOHN,[2] S. JHA,[3] A.L. PILCHAK,[2,4] R. ARROYAVE,[1] and E.J. PAYTON[2]

1.—Texas A & M University, College Station, TX 77818, USA. 2.—Air Force Research Laboratory, Materials and Manufacturing Directorate, Wright-Patterson AFB, OH 45433, USA. 3.—University of Dayton Research Institute, Dayton, OH 45469, USA. 4.—MRL Materials Resources LLC, Xenia, OH 45385, USA. 5.—e-mail: jaylen.james@live.com

The fatigue life of near-alpha titanium alloys in service can be reduced by the presence of clusters of alpha phase with similar *c*-axis orientations, known as micro-textured regions (MTRs) or macrozones. MTRs provide a local environment that facilitates initiation and growth of subsurface cracks. Models exist for the prediction of fatigue crack growth rate, taking into account both dwell time and microtextured region parameters, such as size; however, to date, only 2-dimensional measurements have been used as inputs to this inherently 3-dimensional problem. In the present work, the MTR regions are assumed to have the shape of prolate spheroids, and the major and minor axis lengths are measured in cross-section. Then, the 3D size and shape distributions are estimated using the expectation maximization and the Cruz-Orive spheroid unfolding algorithm. The magnitude of uncertainty in the unfolding results and implications for fatigue life models for Ti-6Al-4V are discussed.

INTRODUCTION

In cold dwell fatigue, growth rates of small cracks are faster in regions of strong local crystallographic texture,[1] resulting in a significant debit in part life.[2] In near alpha-titanium alloys, regions can exist within the microstructure where there are zones of grains with similar crystallographic orientations, known as micro-textured regions (MTRs) or macrozones. They range in size from 100 μm to 10,000 μm, and have been linked to faceted fracture surface morphology.[3,4,5]A key component of The presence of MTRs are a result of the processing history of the alloy.[6]

MTRs within Ti-6V-4Al alloys have been extensively studied leading to a general consensus on what characteristics of MTRs affect crack growth rate. Experiments have shown that these hexagonal close-packed (HCP) α grain regions' influence on crack growth rate can vary, depending on how densely packed these regions are and how closely the *c*-axis direction is oriented along the axis of applied stress.[1] The mechanism by which such cracks are formed has also been studied at length, and has been developed largely upon Stroh's model of a pileup of dislocations at the boundary of an MTR that has its basal plane nearly orthogonal to the loading axis.[7] Although additional physics are required for a complete description of the dwell fatigue phenomenon, the model is frequently referenced in the dwell fatigue literature, and has provided important, foundational insights into the failure mechanism.[8–10] A key component of accurate life prediction includes transferring the physics of the crack growth mechanism into models, and incorporating the most influential attributes of MTRs into such models.

Pilchak developed a model to shed more light on the likelihood of dwell fatigue failure based on the type of loading.[11] An enhancement to this model predicts material life as a function of MTR size, grouping density, and *c*-axis inclination with respect to the loading direction.[12]

The focus of the current work is to understand how much influence 3-dimensional (3D) MTR size has on the predicted dwell fatigue life of Ti-6Al-4V.

(Received April 10, 2022; accepted July 29, 2022)

Published online: 01 September 2022

Prior work has been based exclusively on 2-dimensional (2D) MTR size measurements collected using electron back-scatter diffraction (EBSD). The present work intends to shed light on whether applying stereology to obtain estimates for the major principal semi-axis (MAPSA) of prolate spheroid-shaped MTRs in 3D would create a different result in predicted fatigue life than using the MAPSA lengths of ellipse-shaped MTRs obtained from direct cross-section measurements in 2D, as is the current norm. It should be noted that the present study is purely numerical, since only a comparison between the measurement techniques is needed.

Two stereological approaches, (1) unfolding (UF) and (2) maximum likelihood (ML) via expectation maximization (EM), are used to make estimates of MAPSA lengths in 3D, from 2D data.[13–16] As this is an extreme value problem, we compare the two stereological approaches to assess the degree to which the methodology matters.

The ellipse measurements obtained from a single section of the bulk material consist of random sections of the 3D parent MTRs. As a result, many of the 2D ellipses within the Dataset will originate from intersections of spheroids, where the section is not coincident with the MIPSA of the spheroid. Such an ellipse would have a smaller MIPSA length in 2D than its parent spheroid. Our hypothesis is that the estimation methods will predict longer MIPSA lengths and thus shorter fatigue lives compared to the 2D distribution.

What follows is an explanation of the two approaches employed to estimate 3D size distributions. Next, the methods used to create size estimations of the MTRs in 3D are described. Finally, the lengths are used in a fatigue life model. The results of the study are then shown and discussed.

MATERIALS AND METHODS

Obtaining MTR Measurements

The elliptical dimensions of the MTRs were obtained from a near alpha-titanium alloy, Ti-6Al-4V. The alloy was sectioned in order to analyze the microstructure using EBSD. A combination of the EBSD data and the software DREAM.3D enabled the quantification of 678,963 MTR minor and major principal axis (MAPA) lengths.[17] More information on the criteria chosen to identify MTRs are described in Ref. 3.

Because the specific shape of these regions in 3D can be irregular and distorted due to processing history, it is assumed that the MTRs have the general shape of a prolate spheroid. Simplifying the geometry is also helpful for modeling purposes. A single section of this spheroid would produce an ellipse (excluding the instance where it is sliced coincident with the minor semi-axis, which would produce a circle).

Unfolding (UF)

UF is a stereological technique used to estimate the true, or 3D, size distribution of particles within a body based on a size distribution of the particles from a 2D or 1D section of the body.[18] Since its inception, the numerical approach to UF has been improved upon and modified for different particle geometries. The most frequently assessed situation involves determination of spherical particle size distributions from observations of circular sections.[19]

Another approach to stereological sampling is to take three perpendicular sections of a specimen and, using geometric relationships, infer the 3D shape of the feature. Such an approach is referred to as the tri-sector method.[20] This method is less biased than the dissector method. However, both the dissector and tri-sector approaches are time- and resource-intensive, as many sections must be prepared and characterized. Furthermore, they are destructive to the body being studied. Prior to such techniques, it was clear to mathematicians that the ability to make size estimations of 3D particles from 2D measurements, or to unfold data, from a wider variety of shapes using one section, would be very valuable.

Wicksell was the first to develop an approach to estimating the size–shape distributions of spheroidal particles (3D spheroids) from their ellipsoidal measurements (2D ellipses) using one section. He first did so with spheroidal particles spread throughout a matrix, later expanding the algorithm to include prolate and oblate spheroids.[21,22] Following Wicksell, others began to improve upon his approach and to apply it to specific cases including Cruz-Orive in his work published roughly 50 years later.[23]

In the present work, the 2D MTR data is assumed to be ellipsoidal and therefore prolate spheroidal in shape in 3D.[11] These attributes about our data pointed to the work of Cruz-Orive, who developed a set of equations that can perform UF for oblate or prolate spheroids, given a frequency distribution of MIPSA and minor principal semi-axis (MIPSA) lengths determined by a section of the material.

The output of Cruz-Orive's algorithm, shown in Eq. 1, is a multi-variate histogram of the MIPSA and the eccentricity of the parent spheroids:[13]

$$g_{ij} = (\bar{H}/\Delta)\sum_{\alpha=I}^{s}\sum_{\beta=j}^{k} p^{i,\alpha} * f_{\alpha,\beta} * q^{\beta,j}, (i,j = \overline{1,10}) \quad (1)$$

where $p^{i,\alpha}$ and $q^{\beta,j}$ represent the elements of the size and shape adjustment factors, respectively, and $f_{\alpha,\beta}$ represents the bivariate histogram (m,y^2) where m is the MIPSA of an ellipse and $y^2 = 1-(m/M)^2$ is the unfitness shape component of that ellipse, where M is the largest measured MIPSA length of all the ellipses. The bar over 1,10 denotes the

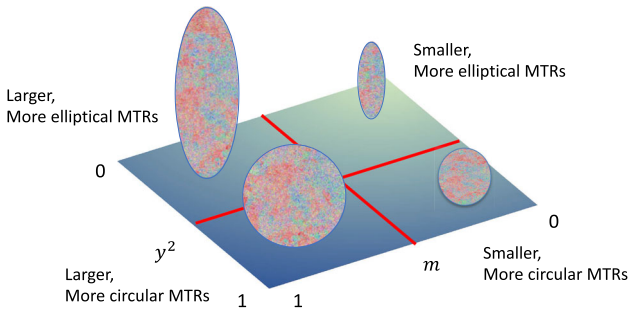

Fig. 1. Form of macrozones, or micro-textured regions (MTRs), with a relationships to region in size–shape space. The macrozones are assumed to be ellipsoidal in two dimensions; m represents the MIPSA length of a macrozones, normalized to the largest value within the experimentally measured set, while the other random variable, y^2, is the unfitness shape component of the ellipse. The colors of the inverse pole figures within the macrozones outlines are for visual appeal only. They do not represent the structure of MTRs in the figure (Color figure online).

selected bin ranges of I and j which, in this case, are from 1 to 10. The random variable ranges are $\{0 < m \leq B\}$ and $\{0, <= y^2 < 1\}$ where B is the largest MIPSA value measured in the Dataset. The variables, s and k, represent the total number of bins of the input histogram for the size and shape components, respectively. The value of each variable is set by the user. $\bar{H}$ represents the overall mean caliper diameter and $\Delta = B/s$. To simplify the analysis, the MIPSA values are normalized, making B equal to 1 and the m value unfitness. For more details on the algorithm, the reader is referred to the source paper.[13] The relationship between y^2, m, and particle morphology is illustrated in Fig. 1.

Once all the elements of the g_{ij} matrix are calculated, a distribution such as that shown in Fig. 2(a and d) is produced. This figure is a reproduction of Cruz-Orive's synthetic input distribution (Fig. 2a and d) and the UF output (Fig. 2b and e) using Python. Both rows in the figure represent the same data viewed from different directions. For the UF histogram, the random variables are labeled x^2 and b. These correspond to the unfitness shape component of a 3D MTR and its MIPSA length, respectively. Furthermore, the shape component, $x^2 = 1 - (\frac{b}{a})^2$, where a is the MIPSA of the spheroid. Given the type of data available and the inferred shape of MTRs, Cruz-Orive's method of UF has been applied. It is from the UF histogram that an MTR's MIPSA can be back-calculated, with the expectation that the estimated value more accurately represents the MTR in 3D.

A major drawback of Cruz-Orive's method is that it is ill-conditioned, meaning that very small changes in the input values can result in large changes in the outputs. This could be due to the complexity of the adjustment factors. Other than editing the formula itself, one can account for the formula's sensitivity by zeroing-out negative bins in the output, which have no physical meaning. Ultimately, the problem of 3D size estimation is one of estimating the parameters of a "hidden" distribution that describes the observable 2D ellipse data. Therefore, the ML via EM was used as an alternative method to compare with the UF method.

First, the eccentricity of each MTR was calculated using its MIPSA and the largest MIPSA length of the Dataset. The values were then binned to create a bivariate histogram, which is subsequently normalized by the sum of the bin frequencies. The input of the algorithm is a bivariate histogram; therefore, the experimental data were binned in such a way that they created a bivariate histogram. The Freedman–Diconis rule was considered to determine the number of bins for each variable.[24] Using the rule, the number of recommended bins was 2113 and 147 for m and y^2, respectively. Together, this would create a bivariate histogram of (2113×147) 310,611 bins. The approximate number of points per cell would be 678,995 points divided by 310,611 bins, resulting in 2.18 points per bin. This value is too small, considering that the purpose of binning is to obtain a general shape of the distribution of data. Another rule-of-thumb for selecting the number of bins for a Dataset is that the average number of data per interval should be greater than the number of intervals. Thus, for the current study, a constant grid size of 20×20 was selected. The effect of bin sizing was not investigated in the present study, and was held constant for all of the calculations.

The input histogram data, provided in Cruz-Orive's paper, was replicated and passed into the UF function, in order to validate the implementation of the code. Figure 2a and b shows the replicated input and corresponding output of Cruz-Orive's algorithm, respectively. Visually, the inputs and outputs from the coded function, and that shown in Fig. 1 in Cruz-Orive's paper, are in very good agreement.[13] Before applying the method to the experimental data, however, it was important to understand how the algorithm performed when the input data did not exactly resemble the synthetic input data supplied by Cruz-Orive. This was done by subsampling the data from a distribution shaped like Cruz-Orive's input distribution.

A sample of values, equal to a predetermined subsample size, was taken, binned, and passed into the UF function. This process was repeated for various amounts of subsample sizes. The result of the test was a continuously decreasing residual sum as the number of input samples was increased. This represents how the UF histogram predictions get closer to the known solution as the input sample size approaches that of the known input.

All the histograms shown in the paper and created with Cruz-Orive's UF function are plotted with any negative bin values set to zero. Although the inputs to Cruz-Orive's UF function ($f_{\alpha,\beta}$) are positive, the adjustment factors can make certain bins in the output (g_{ij}) negative.

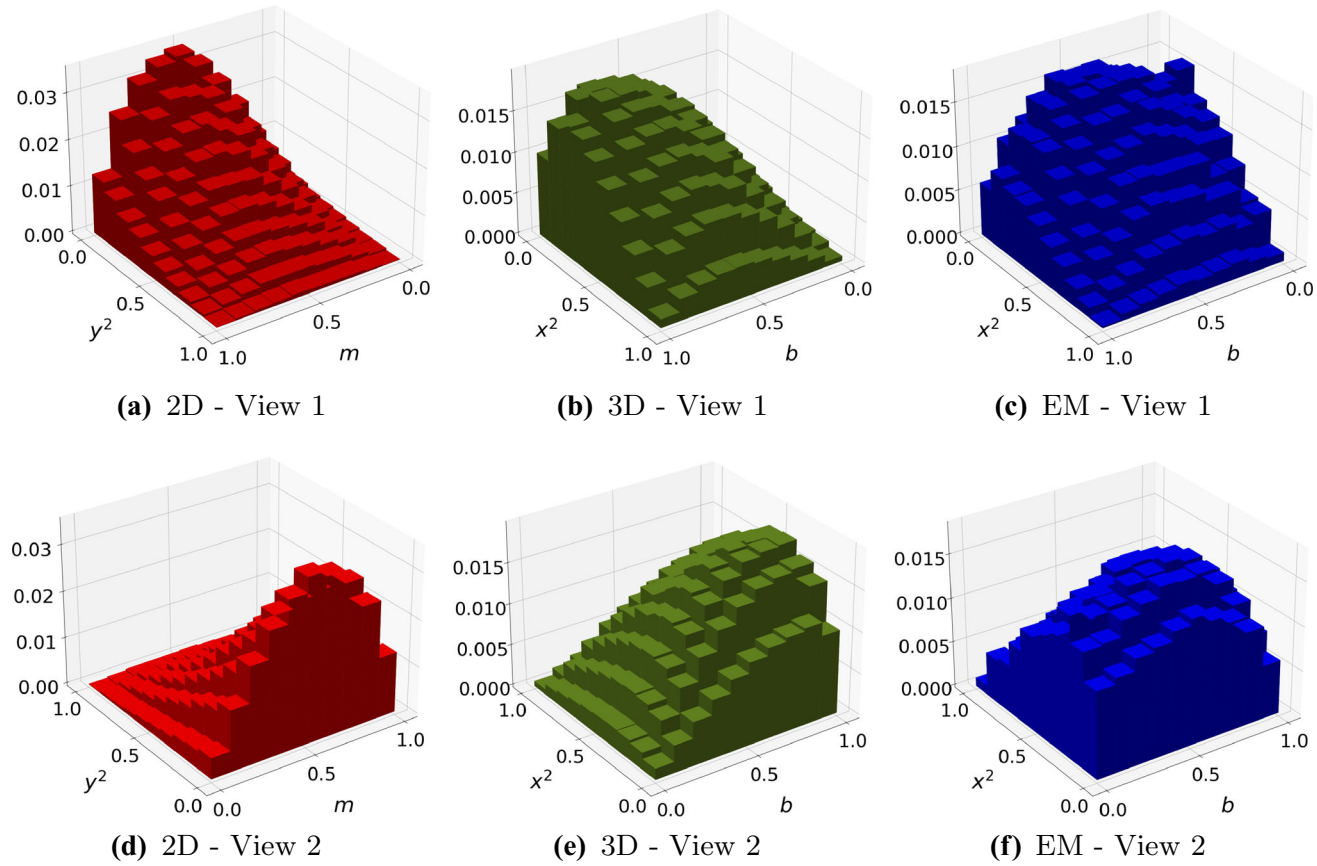

(a) 2D - View 1 **(b)** 3D - View 1 **(c)** EM - View 1

(d) 2D - View 2 **(e)** 3D - View 2 **(f)** EM - View 2

Fig. 2. Bivariate histograms of synthetic ellipse and prolate spheroid eccentricities (y^2 and x^2) and MIPSA lengths (m and b). Two viewpoints are shown for each histogram: (a) and (d) the synthetically generated ellipse data, (b) and (e) the estimated size of prolate spheroids using UF, (c) and (f) the estimated size of prolate spheroids using expectation maximization; the grid size of the histograms is 10 × 10.

Expectation Maximization (EM)

EM employs an iterative optimization technique to determine the parameters of the likelihood function, given a set of observed random variable measurements. In the literature, it is often referred to as the unobservable aspect of an observable set of data. Determining the function is useful for predicting the chance that a random variable will take a particular value in the range of possible values. In maximizing the likelihood, one searches the function parameter space for values that most accurately describe the measured data. An explanation of the EM process and practical examples of applications can be found in Ref. 25.

ML provides a way to estimate the unknown or "missing" function parameters most likely to produce a set of experimental data points. The method can be applied to cases where it is expected that multiple distribution functions are responsible for the observed data.[26] If taking the integral of a likelihood function is intractable, EM can be used to estimate the parameters of the function. When employing EM, it is helpful to select an appropriate likelihood distribution function if there is prior knowledge about the shape of the distribution.

One of the earliest implementations of estimating the likelihood function from incomplete data was by Hartley in 1958. He developed an improved methodology of calculating the underlying parameters of a Dataset (i.e., calculating the ML parameters) with missing data).[27] Later, Dempster et al. followed up Hartley's work by providing the derivation for applying ML to cases when data were missing from a Dataset via EM.[26] Techniques for smoothing the estimation from EM were developed to account for some issues of regular EM which can give "noisy" or "spiky" estimates of the unknown space.[28]

More recently, Baaske et al. studied the estimation of the parameters of a function that described the distribution of spheroids using ML after UF.[15] The distribution, however, is based on a bivariate histogram which is not the most realistic representation of the size–shape distribution of prolate spheroidal-shaped features within a matrix. Studies have shown that the size distribution of MTRs in a near-alpha titanium alloy is not normally distributed. Rather, the distribution is skewed, with smaller major axis and minor axis lengths occurring more frequently than larger ones.[3]

Unlike Baaske et al., Chan and Qin developed an algorithm for applying EM in a non-parametric way.[16] They first considered the case of estimating

the likelihood of a spheroidal distribution using a mixture of 1D, 2D, and 3D data about the spheroidal features. The use of EM helped to overcome the problem of sampling bias and indirect measurements that can come from obtaining lower dimensional measurements from 3D spheroids. Later, in the same work, the authors expand the EM approach to the case of ellipsoidal measurements. This expanded approach is derived from the distribution function describing the size–shape frequency of prolate ellipsoids in a material developed originally by Cruz-Orive.[16]

Different from Cruz-Orive's UF approach, however, the inputs of the Chan and Qin EM algorithm are the individual occurrence probabilities associated with each ellipse measurement. Their EM approach takes the experimental eccentricities and MIPSA lengths as inputs and returns, a probability for each point representing the frequency of observing a given eccentricity and MIPSA length from a 3D prolate spheroid.[16] With each iteration of the EM process, the probability of each ellipse is "adjusted" to more closely reflect that of the 3D size–shape distribution of its parent spheroid. This set of probabilities, along with the corresponding MIPSA lengths and eccentricities, are used to create a discrete distribution where the random variables (MIPSA length and eccentricity) are assigned their newly calculated probabilities. From this distribution, an arbitrarily sized sample of MIPSA lengths and eccentricities can be obtained, and subsequently used to back-calculate MIPSA lengths. For the remainder of the current work, any reference to the EM algorithm will refer specifically to the approach developed by Chan and Qin, unless otherwise stated.

One drawback of the algorithm, however, is that it is memory-intensive when there are a large number of inputs to run. This is because the expectation and maximization steps contain multiple summations using non-trivial functions, making for-loops impractical in terms of script run-time. Converting the formulas into vectors, then summing across the vectors, reduces run-time to reasonable levels. However, this approach requires that the data points be held in the system's random access memory (RAM). The amount of values is on the order of 4.6E11 (or $678,963^2$) which can require hundreds of gigabytes of memory. Please see, for the functional form of the E and M steps, as well as a more detailed explanation of the algorithm.[16]

The largest number of experimental data points that could be run from the total of 678,963 was 400,000; roughly 60% of the data. Therefore, 400,000 data points are uniformly sampled without replacement from the full set of measurements. The subsample included the highest and lowest experimental value from the total Dataset. To run the 400,000 data points, a virtual machine hosted by Google's Cloud computing service was used. The virtual machine had an Intel M1 processor with 3.75 Tb of RAM and a hard drive disk with 7 Tb of storage space.

Prior to the current work, the EM algorithm proposed by Chan and Qin had not been programmed, nor tested.[29] The present implementation of the algorithm was tested using the synthetic Dataset proposed by Cruz-Orive in Ref. 13. The result of the test is shown in Fig. 2c and f). The results compare favorably to Fig. 2b and e, which are the known UF histograms of the synthetic outputs. The residual sum of bin heights between the two histograms was 0.4198 with 200,000 samples of Cruz-Orive's synthetic input histogram.

Sampling from the Distributions

First, the experimental data are binned into a 20 $\times$ 20-celled bivariate histogram. One variable, the MIPSA value (m), is taken directly from the measurements. The eccentricity (y^2) is calculated from the MIPSA and largest MIPSA (M) value of the Dataset.

Next, the bivariate histogram of 2D data is passed into the UF function, resulting in a histogram showing the estimated frequencies of 3D prolate spheroid size–shape classes in the material. The same bivariate histogram of 2D data is passed into the EM function to produce another estimate of the 3D prolate spheroid size–shape distribution. The three histograms can be plotted: one representing the size and shape distributions of the 2D MTR section measurements, one the UF estimates, and the third the EM estimates. Figure 5 displays each of the histograms for the experimental data.

From here, the Numpy random sampling function is employed to sample m and y^2 values from the UF and EM histograms. The sampled MIPSA lengths and shape parameters from each distribution type are used to back-calculate the MIPSA lengths. These lengths, from the 2D measurements, are assigned from the experimental measurements. Each MIPSA length is multiplied by 2 to obtain its MAPA length.

Crack Growth Model

The crack growth rate was modeled using:

$$\frac{da}{dN} = (1 - \chi_I) * \left(\frac{da}{dN}\right)_{cyc} + \chi_I * t_h * \left(\frac{da}{dt}\right)_{dwell}. \quad (2)$$

where χ_I is the indicator function, which is used to determine if the characteristics of a given MTR meet the user defined criteria necessary for it to contribute to accelerated crack growth during dwell fatigue.[12] The dwell time per cycle in seconds is represented by t_h. The first rate term $(\frac{da}{dN})_{cyc}$ is the cyclic small crack growth contribution. Expanded, it has the following form

$$\left(\frac{da}{dN}\right)_{cyc} = e^{C}\Delta K^{n},$$

where C and n are crack growth constants and ΔK is the range in stress intensity factor during the cycle, i.e., $\Delta K = K_{max} - K_{min}$. For an embedded crack in an infinite body, the stress intensity factor K has the form

$$K = (2/\pi) * \sigma * \sqrt{\pi * a},$$

where σ is the applied stress level and a is the crack size. In order to model the small crack growth behavior, an intrinsic crack length parameter, a_{EH}, is introduced. Therefore, ΔK in the cyclic term has the form

$$\Delta K = (2/\pi) * (\sigma_{max} - \sigma_{min}) * \sqrt{\pi * (a + a_{EH})},$$

where σ_{max} and σ_{min} are the maximum and minimum stress levels applied on the material during one cycle, respectively. Due to a_{EH}, the effective ΔK increases when the crack is small, but merges with the ΔK for a long crack when a is significantly larger than a_{EH}. The second rate term, $(\frac{da}{dt})$ is the small crack growth contribution due to dwell time, and is given by

$$\left(\frac{da}{dt}\right)_{dwell} = e^{C_d}K_{max}^{n_d},$$

where C_d and n_d are dwell fatigue crack growth parameters and K_{max} is the maximum stress intensity factor in the cycle. Once again, introducing the parameter $a_{EH,d}$ to account for small crack growth behavior in active MTRs under dwell fatigue, K_{max} has the following form for an embedded crack in an infinite body

$$K_{max} = (2/\pi) * \sigma_{max} * \sqrt{\pi * (a + a_{EH,d})},$$

where $a_{EH,d}$ is the intrinsic crack length parameter associated with the dwell fatigue loading. The χ_I parameter is crucial to incorporating MTR features into the model. With the inclination angle and grouping the density information, it is able to account for anisotropy of the HCP alpha phase where the hardest grains are those with a c-axis parallel to the loading direction and the softest grains are those with a c-axis perpendicular to the loading direction.[9] Grouping density quantifies the concentration of similarly oriented alpha grains within an MTR. Pilchak et al. give more details on how grouping density (or density) is calculated from an EBS image in Ref. 30. However, the crack growth model does not incorporate the path of the crack because correlations to the growth rate and crack path have not been found.[1]

Prior to incorporating data into the crack growth model, two steps are required. First, grouping density values were sampled from a log-normal distribution with a mean and standard deviation of −1.90975 and 0.30897, respectively.[12] Second, c-axis inclination values were generated by sampling from a mixture of two log-normal distributions truncated to range from 0 to 90°.[12] The mean and standard deviation for one of the distributions was 4.22733 and 0.334652, respectively. The second distribution in the mixture distribution had a mean of 3.55245 and standard deviation of 0.726819.

Next, the chi function, χ_I, is constructed using a combination of MAPA lengths, grouping densities, and c-axis inclinations. The bottom half of Fig. 3 shows an example of how these data are used to determine the size and activity of the MTRs. MAPA lengths are represented as horizontal lines. The previously calculated MAPA lengths are set as the lengths of the MTRs. Each length is paired with a grouping density and c-axis inclination. During the χ_I function construction process, a value is randomly selected from the distributions of the c-axis orientation and grouping density variables. A two-state plot is then generated, which represents a crack growing through one MTR (state 1), leaving the MTR, and then entering another (state 2). The lefthand side of Fig. 4 shows this information graphically. For the model, it is assumed that a growing crack is propagating through MTRs at all times. However, not every MTR is active, so growth through inactive MTRs represents the crack growing through a region of the matrix that does not contribute to accelerated crack growth.

If the c-axis inclination is below 30° , with respect to the loading axis and the grouping density above 0.2, then the MTR is considered active, the indicator function value, χ_I becomes 1, and the dwell time effect on crack growth is applied.[12] With χ_I constructed, it can be substituted into the crack growth model in Eq. 2. It is important to note that the illustration on the left side of Fig. 4 simplifies the path of the crack into a straight line. In reality, a propagating crack would not follow such an ideal path. The model compensates for this, however, through the semi-random alignment of active and inactive MTRs.

To calculate the progression of crack growth in the present study, a cycle-by-cycle crack length increment approach was used. The increment in crack length per cycle is given by:

$$\begin{aligned} da = (1-\chi_I) * e^{C} * \\ \left(\frac{2}{\pi} * (\sigma_{max} - \sigma_{min}) * \sqrt{\pi * (a + a_{EH})}\right)^{n} * dN \\ + \chi_I * t_h * e^{C_d} * \\ \left(\frac{2}{\pi} * \sigma_{max} * \sqrt{\pi * (a + a_{EH,d})}\right)^{n_d} * dN. \end{aligned} \tag{3}$$

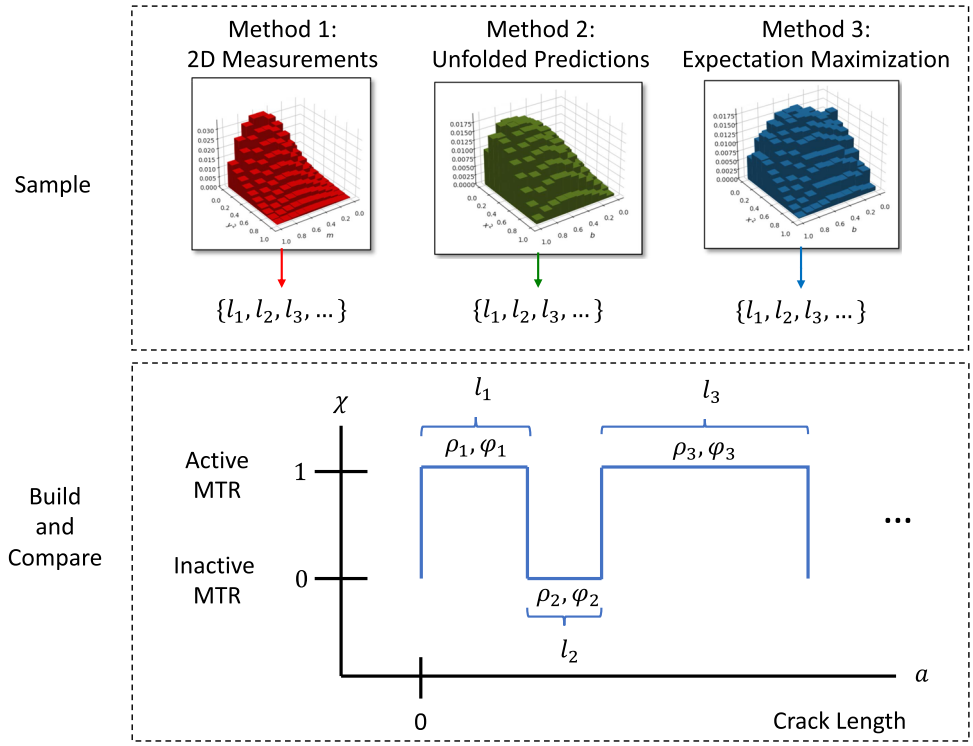

Fig. 3. Method to compare the macrozones size quantification approaches.

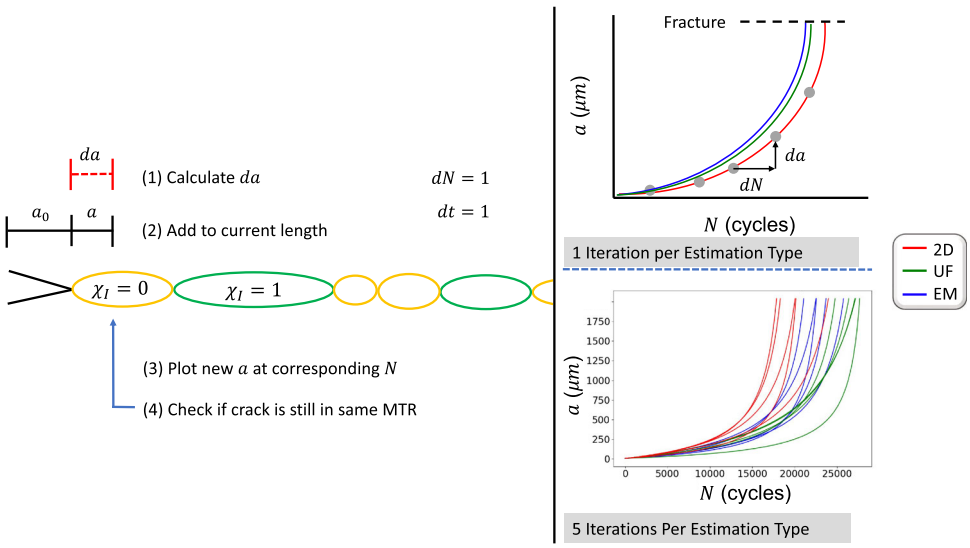

Fig. 4. How the crack growth model plots as curves the crack length, a, against the number of cycles, N.

Equation 3 is used to generate the data of crack length, a, versus number of cycles, N. An illustration of the way the model incorporates data is shown in the top-right portion of Fig. 4. The bottom-right portion of the figure shows an implementation of the model constructing 5 iterations of growth curves from each estimation type. In the present study, two cases of the model were implemented.

In the first case, the χ_I table and every model parameter (C, n, a_{EH}, C_d, n_d, $a_{EH,d}$) are held constant at a deterministic value, that has been selected randomly from the appropriate multivariate normal distributions described below. Here, only the MAPA lengths are updated with each curve. Sampling in this way allows the isolation of the influence of MTR size on dwell fatigue life distribution.

In the second case, the MTR microstructure and the crack growth parameters were considered as random variables in the calculation of each curve. A set of values for C, n, and a_{EH} have been sampled

from a multivariate normal distribution, with means −27.5287, 3.8578, and 4.07E-5, respectively. The co-variance was set to

$$\begin{bmatrix} & C & n & a_{EH} \\ C & 0.338 & & \\ n & -0.0957 & 0.0275 & \\ a_{EH} & -8.518E-6 & 2.288E-6 & 2.7729E-10 \end{bmatrix}.$$

A set of values is also sampled for each of the parameters C_d, n_d, and $a_{EH,d}$ from a multivariate normal distribution, with means −33.8262, 4.0576, and 2.64E-4, respectively. The co-variance of the values is

$$\begin{bmatrix} & C_d & n_d & a_{EH,d} \\ C_d & 0.0042 & & \\ n_d & 0.0073 & 0.0127 & \\ a_{EH,d} & -4.904E-6 & -8.477E-6 & 5.66E-9 \end{bmatrix}.$$

These mean and co-variance values were determined by running multiple small crack growth tests on Ti-6Al-4V fatigue specimens. A model was fit to the small crack growth data to determine the statistics on the model parameters. Note that the means and co-variance distribution parameters used are the same among all the varying length cases. Thus, the exact numerical values used should not influence the final crack growth comparison between the 2D, 3D, and EM estimation types, which is one key aim of the current work. Lengths for a given estimation type are also sampled from the appropriate distributions. Values for grouping density and c-axis inclination are also sampled and assigned to the lengths to build a χ_I table.

In both cases, dN is set to 1 so that each iteration represents 1 cycle. The initial length of the crack was set to 5.4E-6 m (or 5.4 μm) which is half the average alpha particle size in the alloy (half because the initial crack length is measured from the center of the alpha particle).[1] Also, the dwell time, t_h, is set to 118 s. With each iteration, the code also checks if the maximum stress intensity factor, K_{max}, is greater than a critical value, set as 60 MPa $\sqrt{m}$. If it is not, the process repeats. If it is, the process ends.

The crack growth calculation is repeated for each method of MTR size quantification, i.e., a set of a versus N curves is generated for each histogram (2D, UF-based 3D estimation, and EM-based 3D estimation). The final result is a distribution of fatigue life which is informed by the MTR parameters.

RESULTS

Bi-Variate Histograms of MTR Data

The 2D, UF, and EM distributions for the experimental data are shown in Fig. 5. Figure 5(a) shows the bivariate distribution of the more than 600,000 experimental 2D ellipse measurements. As shown, the shape of the histogram is very different than that of Cruz-Orive's synthetic input Dataset (cf. Fig. 2(a and d)).

The histogram data show that each estimation type has a slightly different size distribution of both larger and smaller MTRs. However, the histograms share a similar shape when observed on the MIPSA direction or margin. In each, the largest number of MTRs are small in length fraction (i.e., contained within the m or b bin ranges of 0.0–0.05). Bin heights taper off significantly in the 0.05–0.1 range, and continue to decrease rapidly as bin ranges approach 1. The shape indicates that a very large fraction of the data consist of smaller MTRs.

A major difference between the histograms is the gradient in eccentricities (y^2 and x^2). The histogram displaying experimental data (Fig. 5a and d) has a significant number of eccentricities ranging from 0 to 1 in the m fraction size range of 0.0–0.05. The EM histogram preserves some of this distribution, but does not predict significant bin heights at smaller eccentricities.

According to the Z-axis heights, it is clear that the UF predictions (Fig. 5b and e) have the least spread over the b-x^2 space. Prior to plotting the histograms, the bin heights have been normalized. Because fewer bins occupy cells outside the front right corner of the space (0.0–0.1 b, 0.7–1 x^2), the fraction of sizes contained within it are higher than the 2D and EM histograms. The zeroing-out of bins could be contributing to the added weight (or increased bin height) of non-zero bins. The ill-conditioning of the Cruz-Orive method makes it less robust than the EM approach for making size predictions.

CDFs of Lengths

The cumulative distributions of MTR lengths sampled from each histogram are plotted in Fig. 6. The MIPSA lengths and eccentricities are simultaneously sampled from the appropriate bivariate size–shape distributions in Fig. 5. MIPSA lengths are back-calculated using the MIPSA lengths and eccentricity values, and plotted in Fig. 6b. For each data source, the spread of points in size are a direct result of the bin heights in the corresponding histograms.

Of the three data sources, the UF points are the most sparse in terms of size or shape variation. In each subplot of Fig. 6, most of the UF data appear as discrete bands and are not as "continuous" as the 2D or EM data. The lack of variation is a direct result of having fewer bins to select from during the sampling process. Likewise, fewer bins are a result of negative bins being zeroed-out after UF is applied. The sensitivity of the Cruz-Orive algorithm is not able to handle the non-ideal, experimental data well. Outputs of the model fluctuate significantly if they stray even slightly from the ideal, synthetic input Dataset.

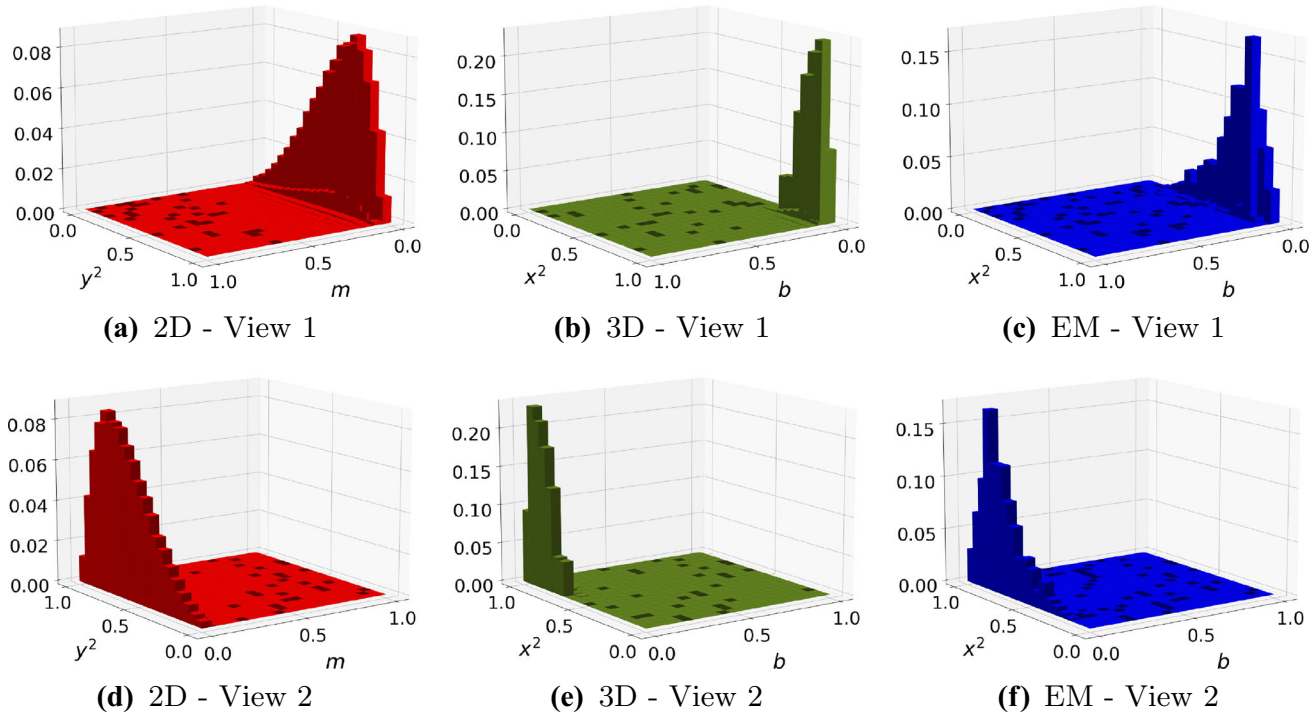

(a) 2D - View 1 **(b)** 3D - View 1 **(c)** EM - View 1

(d) 2D - View 2 **(e)** 3D - View 2 **(f)** EM - View 2

Fig. 5. Bivariate histograms of MTR eccentricities (y^2 and x^2) and MIPSA lengths (m and b). Two viewpoints are shown for each histogram: (a) and (d) the experimentally measured MTR data, (b) and (e) the estimated size of MTRs in 3D using UF, (c) and (f) the estimated size of MTRs in 3D using EM; the grid size of the histograms is 20 × 20.

Figure 6a and b shows the principal semi-axis dimensions of the MTRs. Here, the right tails of the UF and EM estimation types are less populated than the 2D experimental data. This means that the EM and UF methods predict fewer MTRs with principal semi-axis lengths greater than ~ 500 ($\sim 10^{2.7}$) μm compared to the 2D data. The data show that 2D experimental measurements can suggest a greater number of large MTRs in the material than there actually are.

Dwell Fatigue Life Distributions

Figures 7 and 8 summarize the predictions of the number of cycles at failure for each of the three methods. Figure 7 displays a case where only the MTR lengths vary but the crack growth parameters are considered to be deterministic. Figure 8, on the other hand, displays the case where the MTR lengths, the χ_I function, and all the parameters of the crack growth model are considered as random variables for a given estimation type. Both Figs. 7 and 8 plot the life at fracture in the form of a cumulative distribution.

The distribution in life predicted by each estimation type is different. In the first case, where the crack growth parameters are held constant and only the MTR lengths vary (Fig. 7), the 2D and EM estimation types predict similar minimum cycle lives. The UF Dataset, however, predicts a minimum number of cycles that is more than 2,000 cycles less than both the 2D and EM datasets. For the second case, which is a more realistic scenario, where both the MTR lengths and the crack growth parameters are random variables (Fig. 8), there are differences in the median life by the three estimation methods. The difference between the three estimation methods decreases in the upper and lower tails of the distributions. Note that the implementation of the model stops the crack from continuing to grow after 400,000 cycles, but the vertical accumulation of points on the high cycle edge of Fig. 8 shows that more cycles could have been achieved.

B0.1 lines are shown for each of the data sources in both Figs. 7 and 8, as well as the respective inset boxes of the figures. The B0.1 life, or book life, is a statistic used to report the minimum life of a component.[31] The inset boxes emphasize the difference in book life in the lower tail of the distributions. In addition to the B0.1 statistic, the B0.01 and B0.001 statistics are tabulated for both cases in Tables I and II. The B0.1, B0.01, and B0.001 book lives represent the one-thousandth, one-hundredth, and the tenth lowest value of one-million values, respectively. In Table I, in which only the MTR lengths vary, the 2D and EM datasets begin to converge to a similar minimum, while the UF Dataset reaches a lower number of cycles limit than the 2D and EM datasets. In Table II, however, the number of cycles between all three MTR size datasets seem to converge as the B statistic values approach the left tail of the distribution.

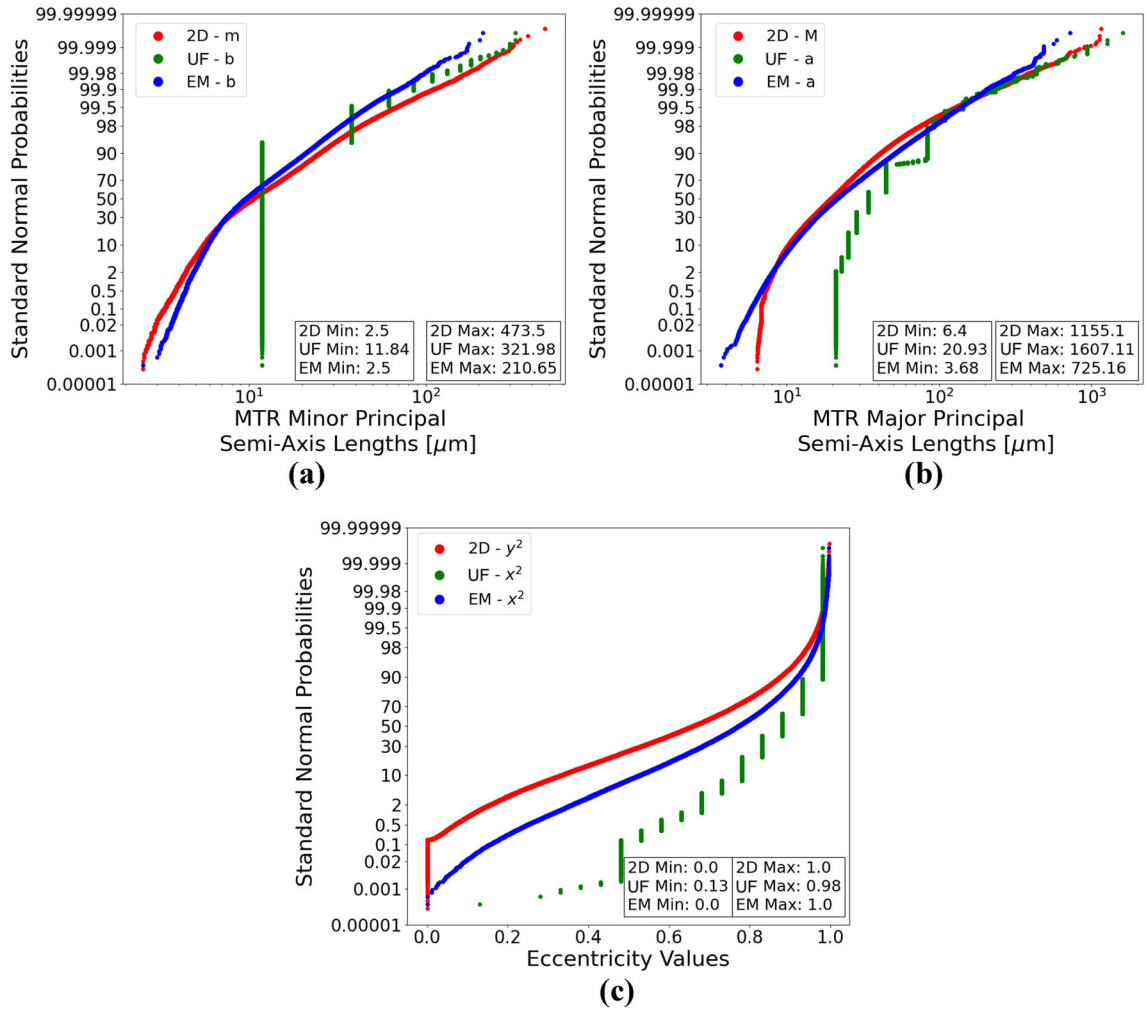

Fig. 6. (a) MAPSAs, (b) MIPSAs, and (c) eccentricities generated by the three estimation types (2D, UF, and EM); the values of UF and EM are from a sample of 400,000 points of their respective histograms.

Overall, however, the slight differences in cycle lives show that the extra cost associated with obtaining the 3D distribution is minor compared to the return of increased precision. The effect of the estimation method is more apparent for the first case, in which the crack growth parameters were held constant and only the MTR size was considered a random variable (Fig. 7). For the case in which both the MTR microstructure and the small crack growth parameters are random variables, the difference in the lower tail of life distribution by the three methods is not significant.

DISCUSSION

According to the B0.1 statistics in the present work, the order of least to greatest life is UF, EM, and then 2D (Fig. 7). In Fig. 8, UF predicts the least life, followed by EM, and then 2D in terms of the B.01 statistic. The difference in lives by the three methods is not significant for this case. The book life order in both plots has a direct correlation with the MTR size lengths. If two sets of consecutive MTR lengths have the same activation per MTR, the set with larger lengths will cause the crack to grow faster compared to the other set. This is because the crack will spend more time in active MTRs. The order of the cycle lives also corresponds with the distribution of MIPSA lengths in Fig. 6b. Here, the UF distribution predicts a greater number of larger MTRs in the size space compared to the 2D and EM distributions. Interestingly, the EM distribution predicts smaller MTRs compared to 2D at the beginning and end of the distribution. However, it predicts larger MTRs for a significant portion of the distribution space between the tails.

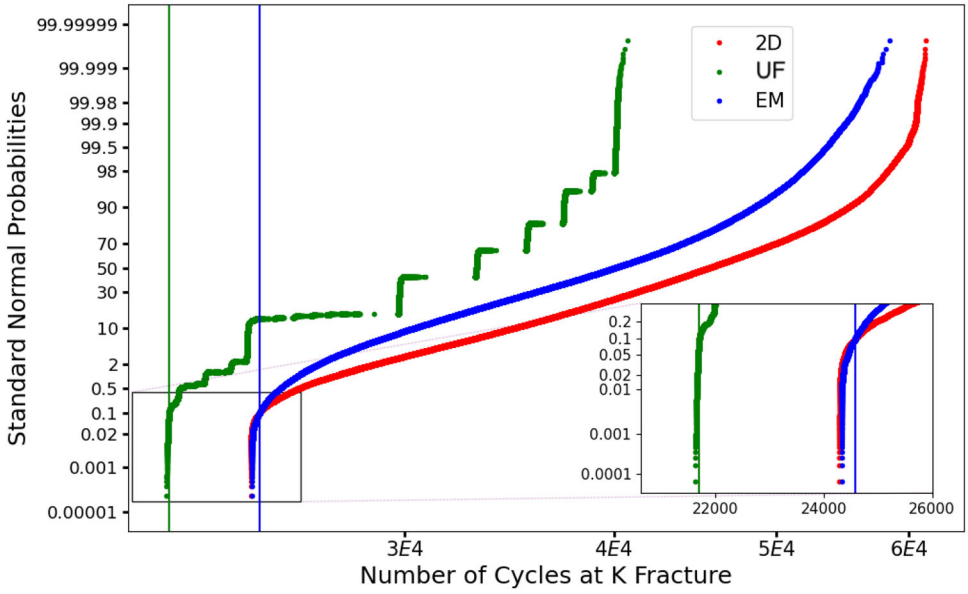

Fig. 7. Cumulative distribution of cycles at fracture predictions for 1 million iterations of *a* versus *N* curves per estimation type. For a given estimation type, only the MTR principal axis lengths vary with each point. The grouping densities, *c*-axis inclinations, and all crack growth model parameters are held constant with each point. Vertical lines are drawn at the B0.1 life value.

The extreme instances of many consecutively long and active MTRs (shortest lives) and many consecutively short and active MTRs (longest lives) are displayed in both Figs. 7 and 8. The clearest influence of these distributions on crack growth is shown in Fig. 7. The ranges of achievable cycles between each estimation type exist between a minimum of about 20,000 and 65,000 cycles. When compared to Fig. 8, the influence of the χ_I function and parameters on fatigue life can be seen, given that the cycle life range for this set of points is between roughly 5,000 and a user-defined maximum of 400,000 cycles. When all the MTR characteristics are allowed to vary, the range of achievable cycle lives greatly increases. With more parameters varying, there are lower minimums as well as higher maximums, compared to the length isolation case of Fig. 7.

Like in Fig. 7, points found near the left edge of Fig. 8 are important to analyze because they represent the shortest life spans of the part. They are the result of a crack growing through a greater number of active MTRs with larger MAPA lengths, causing the crack to grow faster than normal in a given amount of time. In the deterministic case shown in Fig. 7, the 2D and EM B.01 statistics predict considerably more cycles than the UF B.01 statistic. In the case where the crack growth parameters vary, shown in Fig. 8, the predictions of the three B.01 statistics are much closer. However, the 3D estimation approaches (UF and EM) predict shorter B0.1 book lives than the experimental 2D data, by at least 280 cycles. Because the differences in B.01 book life are not substantial for the case where the parameters vary, the differences are not expected to be substantial in practice.

One limitation encountered in the present study was that some MTR lengths captured experimentally approached the step size of the EBS scan. Therefore, measurements with a minor principal axis $(2 * m)$ smaller than 5 μm were removed before conducting the study. Doing so would allow the results to resemble reality more closely. This size filter reduced the data from 678,995 to 678,963 measurements.

Optimizing the code for increased speed created another barrier to calculation, in that a large amount of RAM was required to calculate probabilities over the entire Dataset. To overcome this challenge, the experimental data were down-sampled to 400,000 points before applying the EM algorithm. To capture a representative sample, a uniform sampling scheme without replacement was

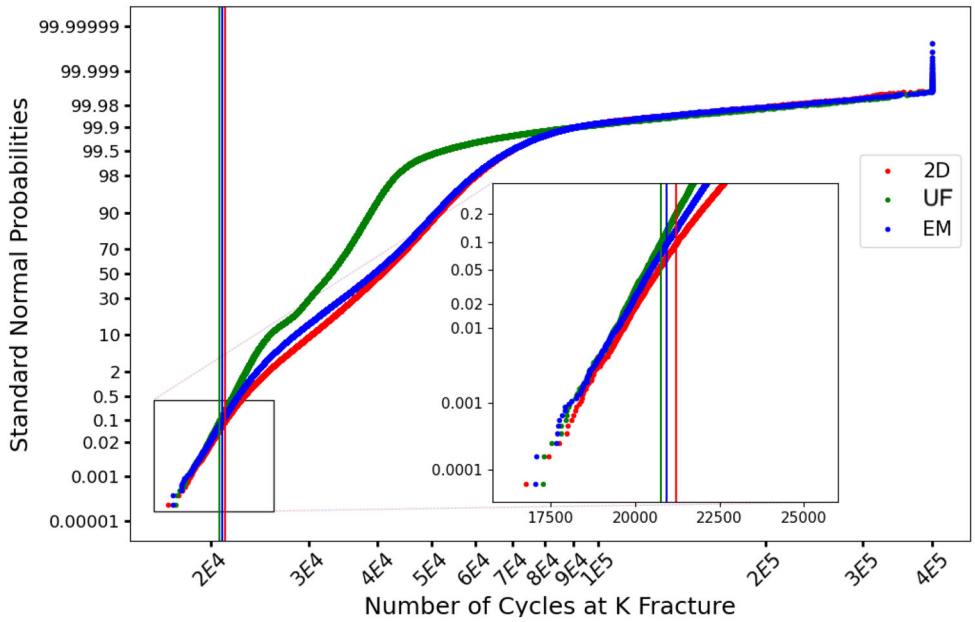

Fig. 8. Cumulative distribution of cycle at fracture predictions for 1 million iterations of *a* versus *N* curves per estimation type. For a given estimation type, the MTR principal axis lengths, grouping densities, c-axis inclinations, and all crack growth model parameters vary with each point. Vertical lines are drawn at the B0.1 life value.

Table I. Important number of cycle statistics for the case in which the grouping densities, c-axis inclinations, and small crack growth parameters are held constant and only the MTR lengths are considered as a random variable

Data source	B0.001 Cycles	B0.01 Cycles	B0.1 Cycles	Median
2D	24,289	24,298	24,588	45,606
UF	21,636	21,661	21,707	33,120
EM	24,330	24,338	24,586	40,066

Table II. Important number of cycle statistics for the case in which the grouping densities, c-axis inclinations, small crack growth parameters, and MTR lengths are considered as random variables

Data source	B0.001 Cycles	B0.01 Cycles	B0.1 Cycles	Median
2D	18,352	19,654	21,230	40,570
UF	18,072	19,403	20,754	32,838
EM	18,020	19,450	20,948	39,253

applied. Fortunately, the extremes of the lengths (min and max) were captured in the subsample and over 58% of the experimental data were used.

CONCLUSION

A comparison of the fatigue life prediction between three different approaches to quantifying the dimensions of MTRs within Ti-6Al-4V is presented. The following are the major conclusions:

- Stereological correction produces systematic shifts in the size, eccentricity, and semi-axis length distributions of the MTRs. The largest influence is observed toward the smaller, more elliptical side of the spheroid distribution.
- While the Cruz-Orive UF algorithm and Chan and Qin EM estimation histograms predict fatigue life similarly when MTR principal axis lengths, grouping densities, and *c*-axis inclinations are all randomly sampled, the EM method should be used due to numerical stability relative to Cruz-Orive's UF algorithm.
- The 3D sizes of MTRs (EM and UF) result in a smaller reduction in predicted fatigue life than the 2D measurements of MTRs measured with EBS. Also, when variability in crack growth behavior is accounted for, by treating the crack growth parameters as random variables, the differences between the three estimation methods decreases substantially compared to a deterministic case, especially in the lower tail of the life distribution.

Future work should analyze the assumption of whether prolate spheroids are the best description of the shape of an MTR, and whether biases exist in the observation of MTR orientation, which could have a significant effect on stereological results. The size and shape of MTRs can vary somewhat with the parameters used to identify them from EBS data. In particular, the edges of the features are not always clearly defined, and the actual shapes are not necessarily rotationally symmetric along the primary axes, as is the case with a prolate spheroid. In some circumstances, where the flow path during deformation processing of the material is curved (not typical of the MTRs in the present work), the globally convex assumption employed in the algorithms in the present work may not be valid, because it is possible that the MTR may also exhibit curvature.

ACKNOWLEDGEMENTS

Funding for this work was provided by the Minority Leaders - Research Collaboration Program under Grant No.FA8650-19-F-5830, located at the Air Force Research Laboratory's Wright-Patterson Air Force Base in Ohio. RA acknowledges support from NSF through Grant No. NSF-CDSE-2001333. Portions of the calculations were carried out at the Texas A&M High Performance Research Computing (HPRC) facility.

CONFLICT OF INTEREST

On behalf of all authors, the corresponding author states that there is no conflict of interest.

REFERENCES

1. A.L. Pilchak, A. Hutson, W.J. Porter, D. Buchanan, and R. John, "On the Cyclic Fatigue and Dwell Fatigue Crack Growth Response of Ti-6Al-4V." In: *Proceedings of the 13th World Conference on Titanium* (V. Venkatesh, A.L. Pilchak, J.E. Allison, S. Ankem, R. Boyer, J. Christodoulou, H.L. Fraser, M.A. Imam, Y. Kosaka, H.J. Rack, A. Chatterjee, A. Woodfield, eds.), 993, John Wiley & Sons, Inc., 2016.
2. D. Norfleet, J. Williams, S. Ghosh, M. Mills, and S. Rokhlin, *The Japan Institute of Metals*(2007).
3. A.L. Pilchak, J. Shank, J.C. Tucker, S. Srivatsa, P.N. Fagin, and S.L. Semiatin, *Integr. Mater. Manuf. Innov.* 5(1), 259 (2016).
4. A.L. Pilchak and J.C. Williams, *Metall. Mater. Trans. A* 42, 1000 (2011).
5. I. Bantounas, D. Dye, and T.C. Lindley, *Acta Mater.* 58, 3908 (2010).
6. Y. Liu and F.P.E. Dunne, *Int. J. Fatigue* 142, 105971 (2021).
7. A.N. Stroh and N.F. Mott, *Proc. R. Soc. Lond. A* 223, 404 (1954).
8. W. Evans and M. Bache, *Int. J. Fatigue* 16(7), 443 (1994).
9. M. Cuddihy, A. Stapleton, S. Williams, and F. Dunne, *Int. J. Fatigue* 97, 177 (2017).
10. Y. Xu, S. Joseph, P. Karamched, K. Fox, D. Rugg, F.P.E. Dunne, and D. Dye, *Nat. Commun.* 11, 5868 (2020).
11. A.L. Pilchak, *Scr. Mater.* 74, 68 (2014).
12. S.K. Jha, J.C. Tucker, J.M. Larsen, R. John, and A.L. Pilchak, The Minerals, Metals, & Materials Society Annual Meeting.
13. L. Cruz Orive, *J. Microsc.* 112, 153 (1978).
14. L.M. Cruz-Orive, *Image Anal. Stereol.* 36, 153 (2017).
15. M. Baaske, F. Ballani, and A. Illgen, *Spatial Statis.* 26, 83 (2018).
16. K.C.G. Chan and J. Qin, *Biometrika* 103(2), 273 (2016).
17. M.A. Groeber and M.A. Jackson, *Integr. Mater. Manuf. Innov.* 3(1), 56 (2014).
18. W.L. Nicholson and K.R. Merckx, *Technometrics* 11, 707 (1969).
19. E.J. Payton, *J. Min. Mater. Charact. Eng.* 11(3), 221 (2012).
20. L.M. Karlsson and A.M. Gokhale, *Acta Stereol* 53 (1996).
21. Wicksell, *Biometrika* 17, 84 (1925).
22. Wicksell, *Biometrika* (1926).
23. L.-M.C. Cruz-Orive, *J. Microsc.* 107, 235 (1976).
24. D. Freedman and P. Diaconis, *Z. Wahrscheinlichk. Verw. Geb.* 57, 453 (1981).
25. C.B. Do and S. Batzoglou, *Nat. Biotechnol.* 26, 897 (2008).
26. A.P. Dempster, N.M. Laird, and D.B. Rubin, *J. R. Stat. Soc. B* 39(1), 1 (1977).
27. H. Hartley, *Biometrics* 14(2), 174 (1958).
28. B.W. Silverman, M.C. Jones, J.D. Wilson, and D.W. Nychka, *J. R. Stat. Soc. B* 52, 271 (1990).
29. K.C.G. Chan., 2021. Private Communication via Email.
30. A.L. Pilchak, J.C. Tucker, and T.J. Weihing, Determining the Probability of Occurrence of Rarely Occurring Microstructural Configurations for Titanium Dwell Fatigue, in *From Microstructure Investigations to Multiscale Modeling*. (Wiley, New York, 2017), pp.41–66.
31. L. Christodoulou and J.M. Larsen, JOM 56, 15 (2004).